Friction **12**(6): 1214–1234 (2024)
https://doi.org/10.1007/s40544-023-0802-2
ISSN 2223-7690
CN 10-1237/TH
RESEARCH ARTICLE

Scuffing failure analysis based on a multiphysics coupling model and experimental verification

Bugao LYU, Xianghui MENG*, Jiabao YIN, Yi CUI, Chengen WANG
School of Mechanical Engineering, Shanghai Jiao Tong University, Shanghai 200240, China
Received: 03 March 2023 / Revised: 08 May 2023 / Accepted: 07 July 2023

Abstract: General reductions in lubricant viscosities and increasing loads in machine components highlight the role of tribofilms in providing surface protection against scuffing. However, the relationship between the scuffing process and the growth and removal of tribofilm is not well understood. In this study, a multiphysics coupling model, which includes hydrodynamic lubrication, asperity contact, thermal effect, tribochemistry reaction, friction, and surface wear, was developed to capture the initiation of surface scuffing. Simulations and experiments for a piston ring and cylinder liner contact were conducted following a step-load sequence under different temperature conditions. The results show that high temperature and extreme load could induce the lubricant film collapse, which in turn triggers the breakdown of the tribofilm due to the significantly increased removal process. The failures of both lubricant film and tribofilm progress instantaneously in a coupling way, which finally leads to severe scuffing.

Keywords: scuffing failure; tribofilm; boundary lubrication; multiphysics coupling effects

1 Introduction

Surface scuffing is a type of catastrophic failure in lubricated mechanical components that occurs suddenly and unexpectedly, progressing rapidly. It is primarily initiated by the breakdown of surface films that protect against extreme operating conditions, leading to large-scale adhesion, welding of sliding interfaces, and severe wear. This problem can arise in many friction pairs, such as gears, cams and followers, piston ring and cylinder liner pairs, and bearings [1, 2]. The mechanism of scuffing is complex and involves multiphysics coupling effects [3, 4], including hydrodynamic lubrication, asperity contact, thermal effects, tribochemistry reactions, friction, and wear. Although various mechanisms have been proposed to explain the onset and progression of scuffing, a universal criterion or reliable model to predict its initiation has yet to be agreed upon.

Research on scuffing has been ongoing for more than eight decades and has led to the development of several proposed mechanisms and predictive theories. The flash temperature theory, introduced by Blok [5], is one of the earliest and widely accepted scuffing criteria. This theory suggests that surface scuffing occurs when the contact flash temperature of a given lubricant and friction pair material combination reaches a critical value. In contrast, Dyson et al. [6] proposed that scuffing initiates when the elastohydrodynamic lubrication (EHL) film collapses due to a critical temperature rise in the contact inlet. This differs from Blok's theory, which suggests that the temperature rise within the sliding contact caused by friction heating is responsible for scuffing. In addition to lubrication, adiabatic shear instability on the near-surface material of the sliding interface is also a key process in scuffing [7, 8]. A corresponding model has been established to express the susceptibility of a sliding contact interface to scuffing in terms of material properties and contact conditions. Tribofilms formed by tribochemistry

* Corresponding author: Xianghui MENG, Email: xhmeng@sjtu.edu.cn

Nomenclature

A	Contact area (m²)
c	Specific heat of lubricant (J/(kg·K))
$c_{a,b}$	Specific heat of substrates (J/(kg·K))
E'_{sub}, E'_{tri}	Equivalent elastic modulus of the substrate and tribofilm (GPa)
F_{fri}, F_{tri}, F_{sub}, F_{lub}	Total, tribofilm contact, substrate contact, and lubricant friction (N)
h	Film thickness (m)
$h_{\mathrm{w}}^{\mathrm{mild}}$, $h_{\mathrm{w}}^{\mathrm{mech}}$	Mild and adhesive wear depth (m)
h_{tri}	Tribofilm thickness (m)
k	Thermal conductivity of lubricant (W/ (m K))
$k_{a,b}$	Thermal conductivity of substrates (W/(m·K))
K	Removal coefficient of the tribofilm ($\mathrm{Pa^{-1}}$)
K_{sub}	Wear coefficient of the substrate ($\mathrm{Pa^{-1}}$)
p_{lub}	Film pressure (Pa)
p_{asp}	Asperity contact pressure (Pa)
t	Time (s)
T	Lubricant temperature (K)
T_0	Ambient temperature (K)
u, v	Velocities of the control volumes in x and y directions (m/s)
U_a, U_b	Velocities of the substrates (m/s)
w	Applied load (N/m)
x	Coordinate in sliding direction
y	Coordinate vertical to sliding direction
z	Coordinate in film thickness direction
ΔU_{act}	Internal activation energy (eV)
ΔV_{act}	Activation volume ($\mathrm{Å}^3$)
α, β, γ, p_0	Parameters of tribofilm removal
β_{T}	Thermal expansion coefficient ($\mathrm{K^{-1}}$)
β_{s}	Asperity radius (μm)
η	Lubricant viscosity (Pa·s)
η_0	Initial lubricant viscosity (Pa·s)
η_{s}	Density of asperities ($\mathrm{\mu m^{-2}}$)
μ_{sub}, μ_{tri}, μ_{adh}	CoFs of substrate, tribofilm, and adhesion
$\rho_{a,b}$	Substrates density ($\mathrm{kg/m^3}$)
σ	Root mean square height (μm)
Γ_0	pre-factor (m/s)
ϕ_x, ϕ_{c}, ϕ_{s}, ϕ_{f}, ϕ_{fs}, ϕ_{fp}	Flow factors

reactions have been confirmed to be essential for the effective lubrication of sliding surfaces, and the absence of this layer has been suggested as the root cause of scuffing [9]. Other scuffing hypotheses include wear debris scoring [10], additive depletion [11], plastic flow [12], and oxidative decomposition of the lubricant [13], among others.

Although there are various explanations, it is widely acknowledged that scuffing, which involves metal-to-metal direct contact, initiates owing to the collapse of protective hydrodynamic lubrication films, followed by the removal of tribofilms. Numerous studies [6] have focused on investigating the factors that lead to the breakdown of hydrodynamic lubrication films, and several scuffing models based on critical temperature and pressure/velocity criteria have been developed [14, 15]. However, the effect of tribofilm formation and removal on scuffing has received less attention, despite the fact that these tribofilms, formed by extreme-pressure (EP) and anti-wear additives, play an essential role in controlling scuffing, particularly for machine components operating in mixed/boundary lubrication regimes [16, 17].

In boundary lubrication, the rubbing surfaces experience insufficient lubrication by fluid films and instead rely on surface-bonded tribofilms formed by lubricant additives to provide protection [18, 19]. These tribofilms are characterized by relatively low friction and sacrificial wear and can effectively enhance anti-scuffing performance. Zinc dialkyldithiophosphate (ZDDP) is among the most effective additives for reducing surface wear and forms a protective tribofilm that minimizes metal-to-metal contact and reduces wear on rubbing surfaces [20, 21]. ZDDP-derived tribofilms are patchy, rough, and pad-like and can have a thickness of up to 200 nm [22, 23]. Extensive efforts have been conducted to investigate the formation mechanism of ZDDP tribofilms and also to identify its role in scuffing prevention [24]. Dorgham et al. [25] suggested that, before the polymerization of short phosphate chains into a phosphate-rich protective film, ZDDP decomposes to form intermediate zinc

sulfide and sulfate species. The widely accepted stress-augmented thermal activation theory for ZDDP tribofilm growth suggests that tribochemistry reactions producing ZDDP tribofilms are promoted by contact pressure/shear stress and lubricant temperature [22, 26]. However, excessive pressure can have adverse effects [27].

According to Bayat and Lehtovaara [28], ZDDP tribofilms may have a pressure threshold above which their stable thickness cannot be maintained, and removal becomes dominant. The removal process is highly nonlinear and dependent on the applied load [27], with ZDDP tribofilms being susceptible to degradation or collapse under extremely high load or temperature [29]. This can result in exposure of substrate materials and massive surface wear, leading to severe lubrication failure such as scuffing [9, 30]. Therefore, the nature and effectiveness of the tribofilms formed on the surface are key factors controlling scuffing failure under boundary lubrication [31, 32]. The time for the final breakdown of the protective tribofilm is inversely dependent on the applied load, and higher contact loads have been shown to result in premature breakdown of the tribofilm [30]. However, the relationship between tribofilm evolution and the scuffing process is not yet fully understood, and there is currently a lack of a model that integrates the multiphysics coupling effects of lubricant film, tribofilm, and scuffing failure.

The occurrence of surface scuffing is influenced by several interrelated factors, including lubrication, contact, heat, tribofilm, friction, and wear. The present study is aimed to model these factors comprehensively and to predict the occurrence of surface scuffing based on a multiphysics coupling model. The friction force, temperature rise, and wear depth under a step-load sequence and different temperatures were simulated using this model and they were compared with experimental results. The effects of applied load and lubricant temperature were discussed. Moreover, the role of tribofilm evolution and breakdown during the scuffing process was revealed.

2 Scuffing prediction model based on multiphysics coupling effects

The scuffing performance is determined by the multiphysics coupling effects, including hydrodynamic lubrication, asperity contact, tribochemistry, thermal effect, friction, wear, etc. Figure 1 illustrates the contact interface including fluid lubrication, tribofilm contact, and substrate contact. As aforementioned, under extreme conditions, like heavy loads and high temperature, these effects will induce the breakdown of oil film and tribofilm, and surface failure, such as scuffing, may occur.

The following multiphysics coupling model comprehensively considers these effects and is aimed to capture the emergence of surface scuffing. Its flowchart of the computation procedures is briefly depicted in Fig. 2 and explained as follows. To begin the computational process, an initial set of parameters including geometry, mechanical and tribochemistry properties, roughness, temperature, sliding speed, and load are inputted. The surface profile and an assumed minimum film thickness are used to determine the distribution of the oil film. The hydrodynamic lubrication and asperity contact models are then used to compute the oil film as well as asperity contact pressures, respectively. The tribofilm thickness and mechanical properties are updated using the tribochemistry reaction model and incorporated into the asperity contact model. The convergence of load balance is verified, and if it is not met, the film thickness is adjusted, and the calculations are repeated. Upon satisfying the convergence criterion, the thermal effect model is solved to obtain the bulk and lubricant temperatures. The tribochemistry reaction temperature, tribofilm properties, and lubricant viscosity are updated. The calculations are then repeated until the convergence criterion for temperature is achieved. The friction force and wear depth are calculated, and the working parameters, such as sliding speed and

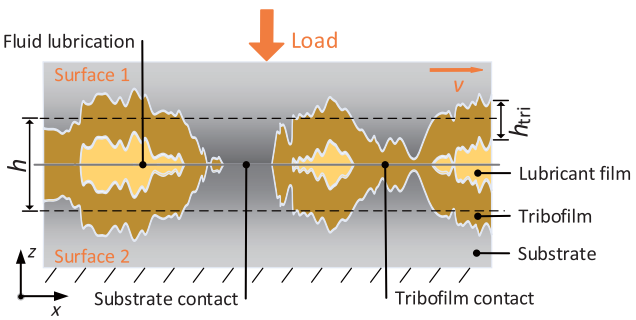

Fig. 1 Schematic diagram of the modeled contact interface.

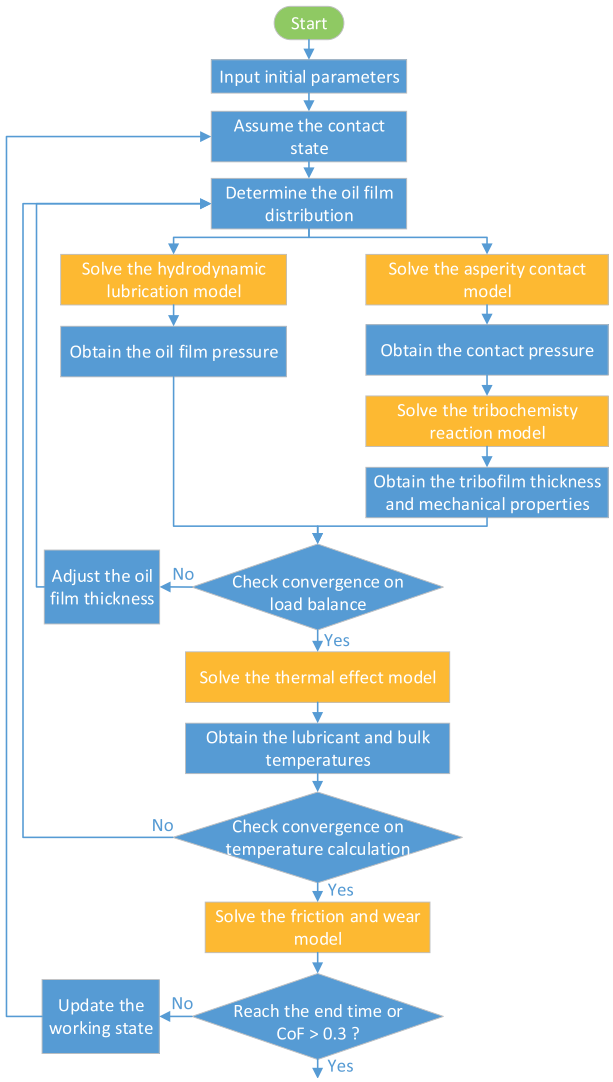

Fig. 2 Flowchart of the computation procedures for the multiphysics coupling model.

applied load, are updated while increasing the simulation time by a specific time step. The computation is stopped when the scuffing initiation is reached, which is recognized as the coefficient of friction (CoF) exceeding 0.3, or when the set time is reached. The subsequent sections will elaborate on these models used in the computations and their interconnections. The following sections will provide further details on these models used in the computations above and their coupling relationship.

2.1 Hydrodynamic lubrication

The hydrodynamic pressure (p_{lub}) of the oil film generated between two rough surfaces is governed by the average Reynolds equation [33] and its two-dimensional form reads as

$$\frac{\partial}{\partial x}\left(\phi_x \frac{h^3}{12\eta}\frac{\partial p_{\mathrm{lub}}}{\partial x}\right)+\frac{\partial}{\partial y}\left(\phi_y \frac{h^3}{12\eta}\frac{\partial p_{\mathrm{lub}}}{\partial y}\right) = \phi_{\mathrm{c}}\left(\frac{U_a+U_b}{2}\frac{\partial h}{\partial x}+\frac{\partial h}{\partial t}\right)+\sigma\frac{U_a-U_b}{2}\frac{\partial \phi_{\mathrm{s}}}{\partial x} \quad (1)$$

where p_{lub} and h are the hydrodynamic pressure and oil film thickness, respectively. η is the lubricant viscosity, U is the sliding velocity in the x direction, t is the time, and σ is the composite surface roughness. ϕ_x and ϕ_y are pressure flow factors along the x and y directions, respectively [33]. ϕ_{s} and ϕ_{c} indicate the shear flow factor and the contact factor, respectively [34, 35]. Note that temperature changes across the film thickness can affect the hydrodynamic pressure by altering the lubricant viscosity across the film. In the present work, the temperature variation across the lubricant film thickness was considered during the thermal effect calculation (see Section 2.2). When solving the Reynolds equation, an average temperature across the lubricant film thickness was used for the sake of computing efficiency. For more accurate results, the generalized Reynolds equation, which considers the temperature variation across the lubricant film thickness, is recommended especially for full TEHL analysis.

The Reynolds boundary condition was used to consider the fluid film cavitation for its high calculation efficiency. It should be acknowledged that the pressure distribution derived by the Reynolds boundary condition may be unphysical especially when the surface is textured or the boundary pressure is high [36]. The Jakobsson–Floberg–Olsson (JFO) [37, 38] boundary condition could be used to ensure the mass conservation and obtain more accurate results. However, for untextured surfaces, the difference in results using the Reynolds boundary condition and JFO boundary condition could be acceptable [36, 39]. The computation cost of JFO boundary condition is much higher than that of Reynolds boundary condition. In the present study, the simulation time is 6 hours (over 200 thousand cycles). Therefore, the Reynolds boundary condition is a reasonable choice to ensure a timely and efficient simulation.

The viscosity of the lubricant plays a crucial role in determining the hydrodynamic pressure and is influenced by both temperature and pressure. To quantify the viscosity, a combination of Vogel's model [40] and Reolands's model [41] is used, which is represented by Eqs. (2) and (3):

$$\eta_0 = a_0 \exp\left(\frac{T_1}{T_2 + T}\right) \tag{2}$$

$$\eta = \eta_0 \exp((\ln \eta_0 + 9.67)[(1 + 5.1\times10^{-9} p_{\text{lub}})^{0.68} - 1]) \tag{3}$$

where T is the lubricant temperature. a_0, T_1, T_2 are parameters related to oil brand.

2.2 Thermal effect and temperature rise calculation

The thermal effect substantially impacts the lubrication performance not only by altering the lubricant properties but also by activating the tribochemistry reaction [26]. The oil film is heated during rubbing due to fluid shear and solid contact friction, resulting in an increase in its temperature as well as the bulk temperature. To model the thermal effect, this study employs three-dimensional energy equations. The energy equation for the oil film is represented as [42]:

$$\begin{aligned} c\rho\left(\frac{\partial T}{\partial t} + u\frac{\partial T}{\partial x} + v\frac{\partial T}{\partial y}\right) &= k\frac{\partial^2 T}{\partial z^2} \\ &\quad -\beta_{\text{T}} T\left(\frac{\partial p_{\text{lub}}}{\partial t} + u\frac{\partial p_{\text{lub}}}{\partial x} + v\frac{\partial p_{\text{lub}}}{\partial y}\right) \\ &\quad +\eta\left[\left(\frac{\partial u}{\partial z}\right)^2 + \left(\frac{\partial v}{\partial z}\right)^2\right] + Q_{\text{asp}} \end{aligned} \tag{4}$$

k, β_{T}, and c denote the thermal conductivity, thermal expansivity, and specific heat, respectively. The fluid velocities in the x and y directions are represented by u and v, while z indicates the coordinate across the oil film. The heat produced by solid contact friction is denoted by Q_{asp} and can be calculated as Eq. (5):

$$Q_{\text{asp}} = \frac{\mu_{\text{asp}} p_{\text{asp}} |U_a - U_b|}{h} \tag{5}$$

μ_{asp} is the CoF of asperity contact, and p_{asp} represents the solid contact pressure.

The energy equations used to determine the temperatures in the contacting solids a and b are given by

$$\begin{cases} c_a\rho_a\left(\dfrac{\partial T}{\partial t} + U_a\dfrac{\partial T}{\partial x}\right) = k_a\dfrac{\partial^2 T}{\partial z_a^2} \\ c_b\rho_b\left(\dfrac{\partial T}{\partial t} + U_b\dfrac{\partial T}{\partial x}\right) = k_b\dfrac{\partial^2 T}{\partial z_b^2} \end{cases} \tag{6}$$

where $c_{a,b}$, $\rho_{a,b}$, and $k_{a,b}$ are the heat capacity, density, and thermal conductivity of the solids a and b, respectively. The heat flux continuity conditions on the oil–solid interfaces connect the oil film temperature and solid temperatures and are given by

$$\begin{cases} k\dfrac{\partial T}{\partial z}\Big|_{z=0} = k_a\dfrac{\partial T}{\partial z_a}\Big|_{z_a=0} \\ k\dfrac{\partial T}{\partial z}\Big|_{z=h} = k_b\dfrac{\partial T}{\partial z_b}\Big|_{z_b=0} \end{cases} \tag{7}$$

The boundary conditions for Eqs. (4) and (6) can be determined as: at $x = x_{\text{in}}$, $z_a = d$, and $z_b = d$, $T = T_0$, $T_1 = T_0$, and $T_2 = T_0$, respectively. Here, d represents the thickness of thermal layers in both solids, while T_0 refers to the ambient temperature. Further details about numerical solutions of the thermal model in Eqs. (4)–(7) can be found in Ref. [43].

In the present study, the ambient temperature (T_0) is determined by the heating system of the tribometer and kept constantly. Then the bulk temperature rise of the liner segment can be solved using the energy equations (Eqs. (4)–(7)) and it is compared with the measured values by a thermocouple beneath the contacting surface. A schematic description of the model to calculate the bulk temperature rise is shown in Fig. 3.

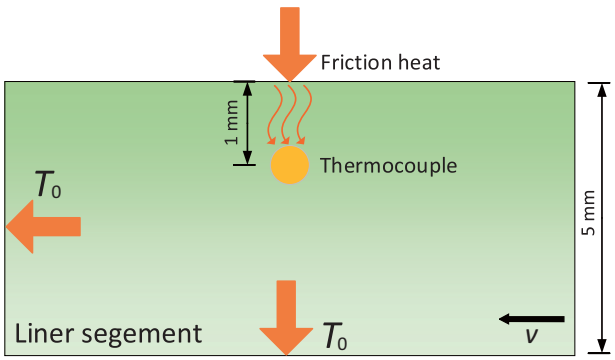

Fig. 3 The model of the bulk temperature rise calculation.

2.3 Asperity contact

Studies showed that ZDDP tribofilms formed on the substrate surface is rough, patchy, and pad-like, the substrate are partly and unevenly covered by the tribofilm [18]. ZDDP tribofilms can mitigate surface wear by reducing direct substrate-to-substrate contact. However, for rough surfaces, substrate-to-substrate contact is inevitable because asperities could penetrate the tribofilm (lower hardness) to contact with the substrate locally, especially for engineering friction pairs whose surface roughness is much higher. Thus, the substrate-to-substrate contact and tribofilm-to-tribofilm contact coexist (see Fig. 1). The contact state changes as the tribofilm thickness evolves during rubbing. In the present study, a layered statistical contact model is employed, which was previously published [27]. It incorporates the statistical characteristics of rough surfaces, the separation distance of two rough surfaces, and the thickness and mechanical properties of tribofilm. This model is illustrated in Fig. 4 and briefly described in this section.

According to the rough surface contact model proposed by Greenwood and Tripp (GT model) [44], the substrate asperity contact pressure (p_{sub}) is given as

$$p_{sub}(h)=\frac{16\pi}{15}\left(\eta_s\beta_s\sigma\right)^2\sqrt{\frac{\sigma}{\beta_s}}E'_{sub}\int_h^{\infty}(z-h)^{2.5}\phi(z)\mathrm{d}z \quad (8)$$

where the probability density function of asperity height is denoted by $\phi(z)$, E'_{sub} represents the equivalent elastic modulus of the substrate material. The composite surface roughness, the asperity density, and the asperity radius are denoted by σ, η_s, and β_s, respectively. The values of these parameters for a specific friction pair are obtained by the method in Appendix and provided for Section 3.1.

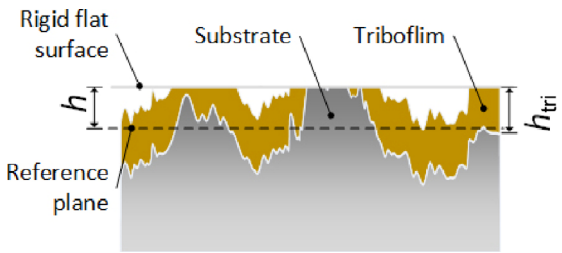

Fig. 4 The schematic diagram of the layered contact model.

In the presence of ZDDP tribofilms, in addition to substrate-to-substrate contact, tribofilm-to-tribofilm contact also occurs, as shown in Fig. 1. The contact state of the tribofilm is directly affected by its thickness (h_{tri}), and the contact pressure of the tribofilm (p_{tri}) is a function of h_{tri}, which is given as

$$p_{tri}(h)=\frac{16\pi}{15}(\eta_s\beta_s\sigma)^2\sqrt{\frac{\sigma}{\beta_s}}E'_{tri}\int_{h-h_{tri}}^{h}(z-h)^{2.5}\phi(z)\mathrm{d}z \quad (9)$$

In Eq. (9), the integration from $(h-h_{tri})$ to h represents the contact fraction of the tribofilm, which can be calculated by subtracting the contact fraction of the substrate (from h to ∞) from the total contact area (from $(h-h_{tri})$ to ∞). Note that an important assumption that the tribofilm is a linear elastic material is made to adapt the GT model for the tribofilm contact calculation. The elastic modulus of ZDDP tribofilms under different temperatures is obtained from Ref. [45], which used a ZDDP-containing base oil. In the present study, a fully-formulated oil was used, and the tribofilm formed at the interface has not only ZDDP in its composition due to the synergistic interactions with other additives. Thus, the mechanical and friction properties of the tribofilm are quite complicated and should be a combination of the properties of the other additives. Unfortunately, to the authors' best knowledge, there is no published experimental data on the variations of mechanical properties of ZDDP tribofilms formed by a fully-formulated oil under different temperatures. It was therefore chosen to use the elastic modulus from Ref. [45] in the present work. To get a better quantitative description, one would need to evaluate the elastic modulus at various temperatures and thicknesses under specific experimental conditions.

The whole asperity contact pressure (p_{asp}) is obtained by summing up the substrate and tribofilm contact pressures:

$$p_{asp}=p_{sub}+p_{tri} \quad (10)$$

The contact model is logical and it depicts the process that the tribofilm will bear more and more applied load as it grows thicker, and the substrate-to-substrate contact is then mitigated.

Another key equation that must be fulfilled is the load balance equation, which guarantees that the

pressures originating from both the fluid and asperities balance the imposed load. The load balance equation is expressed as Eq. (11):

$$w = \iint_A (p_{\text{lub}} + p_{\text{asp}}) \mathrm{d}A \tag{11}$$

In the load balance equation, w represents the applied load, and A represents the contact area. This equation is crucial in ensuring that the solution for both hydrodynamic and contact pressures satisfies physical constraints and the calculated pressures are the true physical pressures.

2.4 Tribochemistry reaction

A high lubricant temperature and contact pressure, according to stress-augmented thermal activation theory, could promote the tribochemistry reaction of the lubricant additive and substrate material to form ZDDP tribofilms. During surface rubbing, the tribofilm is consistently removed and replenished, and the balance between these two processes determines the thickness of the tribofilm. Under an extremely high load or temperature, the removal rate increases nonlinearly and could exceed the growth rate, resulting in a thinner tribofilm and a higher risk of scuffing.

2.4.1 Tribofilm growth and removal

Localized contact shear stress generates frictional energy that leads to chemical reactions resulting in the formation of tribofilms at the contacting interface. Over the years, various methods have been proposed in the literature to capture this tribochemistry reaction, including those presented in references [22, 26, 46]. In this study, we utilize the tribofilm growth model of Zhang and Spike [22] to simulate this interfacial tribochemistry reaction. The growth rate of ZDDP tribofilms $\left(\left(\frac{\partial h_{\text{tri}}}{\partial t}\right)_{\text{gro}}\right)$ is calculated using the stress-activated Arrhenius equation [22]:

$$\left(\frac{\partial h_{\text{tri}}}{\partial t}\right)_{\text{gro}} = \Gamma_0 \exp\left(-\frac{\Delta U_{\text{act}} - \tau \cdot \Delta V_{\text{act}}}{k_{\text{B}} T}\right) \tag{12}$$

$$\tau = \mu_{\text{asp}} p_{\text{asp}} \tag{13}$$

where Γ_0 represents the pre-factor, k_{B} is Boltzmann's constant, ΔU_{act} represents the internal activation energy, ΔV_{act} is the activation volume, and τ is shear stress [22]. The parameters in Eq. 12 (ΔU_{act} and ΔV_{act}), which determines the tribofilm growth rate, were previously calibrated by fitting the experimental results as a formulated lubricant (10W40) was used [27]. It should be noted that elastohydrodynamic lubrication (EHL) pressure and viscous shear can be sufficiently high to form ZDDP tribofilms. Zhang and Spikes et al. [22, 47] studied the formation of ZDDP tribofilms in full-film EHL conditions and suggested that the formation of ZDDP tribofilms does not require solid-to-solid rubbing contact, but is driven simply by applied shear stress. They also found that ZDDP only formed a tribofilm from the fluid with high EHL friction and that this occurred at shear stresses above about 150 MPa [22]. In the present study, we focused on a piston ring and cylinder liner (PRCL) friction pair whose contact is conformal. The hydrodynamic pressure in the lubricated region is significantly lower than EHL conditions and is not high enough for tribofilm formation. Therefore, we only considered the tribofilm formation stemmed from asperity contact with higher pressure and shear stress.

The removal of the tribofilm is known to increase proportionally to its thickness, which is owing to the difference in wear resistance between the free surface (with lower hardness) and the bulk of the substrate (with higher hardness). Additionally, the collapse of tribofilm under high contact pressure has been observed in experiments, leading to the possibility of scuffing failure [26, 28]. To address these effects, a modified tribofilm removal equation has been proposed by the authors in a previous study. This equation is based on Archard's wear model and includes a variable wear coefficient and a multiplication factor that reflects the state of asperity contact [27]. The tribofilm removal rate $\left(\left(\frac{\partial h_{\text{tri}}}{\partial t}\right)_{\text{rem}}\right)$ is given by Eqs. (14) and (15):

$$\left(\frac{\partial h_{\text{tri}}}{\partial t}\right)_{\text{rem}} = K U p_{\text{asp}} \tag{14}$$

$$K = K_{\text{sub}}(1 + \alpha h_{\text{tri}}) \left[\beta \left(\frac{p_{\text{asp}}}{p_0}\right)^{\gamma} + 1\right] \tag{15}$$

where K is the removal coefficient of the tribofilm, K_{sub} is the wear coefficient of the substrate, and α is

a constant describing the change of wear resistance inside the tribofilm. The multiplication factor $\left[\beta\left(\frac{p_{asp}}{p_0}\right)^{\gamma}+1\right]$ is a highly nonlinear term and depends on the contact pressure, with β and γ being constants, and p_0 relating to the contact state. These parameters require calibration through experimentation. Under mild contact states where p_{asp} is low, the multiplication factor approaches 1. Equation (14) predicts a tribofilm removal rate that is similar to the linear equation (without the multiplication factor) used in previous studies [48, 49]. However, for severe contact conditions, Eq. (14) predicts substantially higher removal rates, dozens of times greater than the linear equation, enabling the capture of the initiation of tribofilm breakdown.

The net growth rate of the tribofilm thickness, denoted as $(\frac{\partial h_{tri}}{\partial t})$, can be obtained by subtracting the removal rate from the growth rate:

$$\frac{\partial h_{tri}}{\partial t}=\left(\frac{\partial h_{tri}}{\partial t}\right)_{gro}-\left(\frac{\partial h_{tri}}{\partial t}\right)_{rem} \tag{16}$$

2.4.2 *Tribofilm properties*

The wear coefficient and contact pressure of ZDDP tribofilms are influenced by their mechanical properties, which in turn affect the tribofilm removal rate. Previous studies [30, 50, 51] have shown that the hardness of the tribofilm decreases linearly with its thickness. As the tribofilm grows, its hardness and wear resistance decrease accordingly. To consider this variation in hardness, this study utilizes the equation proposed by Taylor [52].

A high temperature could activate the tribochemistry reaction to form ZDDP tribofilms, but studies [45, 53] have shown that the hardness and Young's modulus of ZDDP tribofilms became lower with the increasing temperature, and at temperatures above 220 °C, the tribofilms begin to degrade [54]. Due to high temperatures, the mechanical properties of the tribofilm can be weakened [53], resulting in reduced wear resistance. To address this, Akchurin and Bosman [55] proposed a compensation factor, enabling the determination of the hardness of the tribofilm at a specific temperature. The Young's modulus of the tribofilm is dependent on its hardness and exhibits a linear increase with hardness beyond a threshold value.

2.5 Friction and wear evaluation

Considering the hydrodynamic lubrication, tribofilm and substrate contacts, the total friction force F_{fri} is contributed by these three parts, i.e., the lubricant shear force F_{lub}, the tribofilm contact friction force F_{tri} as well as the substrate contact friction force F_{sub}:

$$F_{fri}=F_{tri}+F_{sub}+F_{lub} \tag{17}$$

The tribofilm and substrate contact friction forces F_{tri}, F_{sub} are obtained as

$$F_{tri}=\iint_A \mu_{tri}p_{tri}\mathrm{d}A \tag{18}$$

$$F_{sub}=\iint_A \mu_{sub}p_{sub}\mathrm{d}A \tag{19}$$

Here, μ_{tri} and μ_{sub} represent the coefficients of friction of the tribofilm and substrate, respectively. The values of p_{tri} and p_{sub} are determined based on the layered statistical asperity contact model (as discussed in Section 2.3). In this study, the CoF of ZDDP tribofilms is determined through experimental calibration, and it shows minor fluctuations within the temperature range of 60–100 °C [56]. The CoF of the substrate is determined through sliding tribotest without lubricants. It should be noted that once the tribofilm is removed under extreme conditions, metal-to-metal contact would occur in the previously covered areas. It would lead to adhesion contact and a rapid increase in friction force, as the CoF of adhesion contact is much higher than that of tribofilm contact.

The lubricant frication force, F_{lub}, is determined as Eq. (20):

$$F_{lub}=\iint_A\left[\left(\phi_f+\phi_{fs}\right)\frac{\eta U}{h}+\phi_{fp}\frac{h}{2}\frac{\partial p_{lub}}{\partial x}\right]\mathrm{d}A \tag{20}$$

where the terms ϕ_f, ϕ_{fs} and ϕ_{fp} are friction-induced flow factors [33, 34]. p_{lub} is calculated using the average Reynolds equation as described in Section 2.1.

The tribofilm partially and unevenly covers the substrate due to its rough, patchy, and pad-like features

[18], and as a result, substrate contact is inevitable. Therefore, the wear of the substrate material originates from two sources: mild wear due to tribofilm removal and adhesive wear due to substrate-to-substrate contact. The former is caused by the diffusion of substrate atoms into the tribofilm, which are subsequently lost by tribofilm removal. The loss of the substrate material owing to tribofilm removal is obtained based on the combination of the concentration of substrate atoms inside the tribofilm and the tribofilm wear volume. The concentration of the substrate atoms is higher near the substrate–tribofilm interface and lower as the tribofilm grows. Therefore, as the tribofilm thickness increases, the loss of substrate material by tribofilm removal ($h_{\mathrm{w}}^{\mathrm{mild}}$) will decrease [55]:

$$h_{\mathrm{w}}^{\mathrm{mild}} = \int \exp(-c_{\mathrm{m}} h_{\mathrm{tri}}) \left(\frac{\partial h_{\mathrm{tri}}}{\partial t} \right)_{\mathrm{rem}} \mathrm{d}t \tag{21}$$

where the term $\exp(-c_{\mathrm{m}} h_{\mathrm{tri}})$ is the concentration of substrate atoms inside the tribofilm and c_{m} is a constant which is determined experimentally [55].

Adhesive wear ($h_{\mathrm{w}}^{\mathrm{mech}}$) is caused by direct substrate contact and can be assessed using Archard's wear model [57]:

$$h_{\mathrm{w}}^{\mathrm{mech}} = \int K_{\mathrm{sub}} U p_{\mathrm{sub}} \mathrm{d}t \tag{22}$$

ZDDP tribofilms can effectively protect the substrate surface by minimizing substrate contact and preventing adhesive wear. Under mild wear regimes, the rubbing surfaces suffer from only slight damage, and surface wear proceeds steadily with a low wear rate. However, severe wear could emerge due to the dominant adhesive wear once the tribofilm breaks under a much higher load. In this situation, surface failure, such as scuffing, might occur.

In the tribochemistry model, there are some key parameters that require calibration before predictions of surface wear and friction force can be made. They were determined using experimental results for a given operating condition and then used for all other simulations under different conditions. The calibration experiment was conducted under the lubricant temperature of 90 °C and load of 160 N. In the present study a formulated oil (10W40) was used, which is a mixture of base oil with other additives, including detergents, dispersants, and friction modifiers [30, 58]. These additives will compete with ZDDP to adsorb on the sliding surfaces, slowing down the formation of ZDDP tribofilm. Therefore, the parameters used in the growth equation of ZDDP tribofilms (ΔU_{act} and ΔV_{act}) were calibrated by fitting the simulated tribofilm thickness with the measured tribofilm thickness (details can be found in Ref. [27]). In the tribofilm removal equation, K_{sub} (the wear rate of the substrate) and α were determined based on the wear depth and tribofilm thickness measurements. As for β and γ, which are the parameters in the multiplication factor $\left[\beta \left(\frac{p_{\mathrm{asp}}}{p_0} \right)^{\gamma} + 1 \right]$ in the tribofilm removal equation, were obtained from our previous work [27]. In Ref. [27], a set of boundary lubrication experiments was conducted under a wide range of applied load corresponding to various contact states. The tribofilm thicknesses were measured and compared with simulated results to calibrate β and γ. The parameters used in the tribochemistry model are listed in Table 1.

Table 1 Parameters used in the tribochemistry model.

Label	Value
CoF of substrate surface, μ_{sub}	0.15
CoF of ZDDP tribofilm, μ_{tri}	0.11
CoF of adhesion, μ_{adh}	0.5
Wear coefficient, K_{sub} (Pa^{-1})	1.43×10^{-16}
Internal activation energy, ΔU_{act} (eV)	0.711
Activation volume, ΔV_{act} ($\mathrm{Å}^3$)	89
pre-factor, Γ_0 (m/s)	0.01
Parameter of tribofilm removal, α (nm^{-1})	0.21
Parameter of tribofilm removal, β	24.86
Parameter of tribofilm removal, γ	11.96
Parameter of tribofilm removal, p_0	$p_{\mathrm{asp},h=0}$

3 Scuffing experiments and surface characterization

A series of tests were conducted using a step-load sequence under different temperatures to capture the initiation of scuffing failure and obtain the scuffing load. The present model was then used to perform

simulations using input parameters that were consistent with the corresponding tests, and the predicted results were compared to the experimental results. The surfaces were further characterized to analyze the scuffing.

3.1 Test materials

In this study, an experimental simulation was conducted on a piston ring and cylinder liner (PRCL) contact used in an internal-combustion engine typically prone to scuffing failure. The top compression piston ring, with a diameter of 110 cm, was segmented, and a spheroidal graphite cast cylinder liner was sectioned into 1.1° segments in the circumferential direction (about 10 mm arc) and 15 mm in the axial direction. The liner sample has a flat bottom surface with a thickness of 5 mm and a curved top surface that conforms to the piston ring. The surface roughness both of the piston ring and liner samples was measured using a tactile surface profiler (Mitutoyo CV-4500S4). The mechanical and thermal properties as well as surface roughness of the piston ring and liner samples are listed in Table 2. A ZDDP contained mineral engine oil (10W40) was utilized in the experiment, and its properties are provided in Table 3. It is worth noting that studies showed that fully-formulated oils containing polymeric viscosity modifier additives, as is likely the case of the 10W40 oil used in the present work, can exhibit non-Newtonian behavior (shear-thinning effect) from relatively low shear rates, as those verified in piston rings–cylinder liner conjunctions and engine bearings [59, 60].

Table 2 Properties and surface roughness of the piston ring and liner.

Label	Piston ring	Liner
Young's modulus, E (GPa)	155	205
Hardness (HV)	2,000	370
Poisson's ratio, λ	0.3	0.3
Thermal conductivity, $k_{a,b}$ (W/(m·K))	25	55
Heat capacity, $c_{a,b}$ (J/(kg·K))	470	460
Density, $\rho_{a,b}$ (kg/m^3)	7,700	7,200
Surface roughness, σ (μm)	0.416	0.627
Asperity radius, β_s (μm)	7.46	7.57
Asperity density, η_s (μm^{-2})	0.052	0.038

Table 3 Properties of the lubricant.

Label	Value
Viscosity, kinematic at 40 °C (cSt)	100.9
Viscosity, kinematic at 100 °C (cSt)	15.1
Viscosity index	157
Density at 20 °C, ρ (kg/L)	0.861
Thermal conductivity, k (W/(m·K))	0.14
Specific heat, c (J/(kg·K))	1,985
Thermal expansion coefficient, β_T (K^{-1})	6.4×10^{-4}
Flash point (°C)	220
Zinc (wt%)	0.14
Phosphorus (wt%)	0.12

3.2 Test rig and procedure

The ring-on-liner contact experiments were carried out using a reciprocating tribometer (MFT-R4000), and an illustration of the contact is presented in Fig. 5. The liner segment was immersed in the oil bath, and the ring segment oscillated against it with a 10 mm stroke length. The reciprocation frequency was 10 Hz, leading to an average speed of 0.2 m/s during each stroke. A conformal ring holder was utilized to avoid any tilt in the counter-body. Prior to each test, the lubricant was filled in the bath to completely cover the ring-on-liner contact interface, ensuring fully flooded lubrication. The lubricant temperature was maintained consistently by the high-precision heating system beneath the oil bath to avoid any noticeable temperature fluctuations.

Prior to each test, a 30-minute running-in process was carried out under a load of 20 N and a temperature of 30 °C. All tests followed a step-load sequence, as shown in Fig. 6. The load was increased once an hour as it was reported that ZDDP tribofilms could attain a stable state after one hour of rubbing [25] and become nanocrystalline and also more durable [61]. The tests were conducted under three different temperatures, i.e., 60, 100, and 140 °C. It is well-known that surface roughness undergoes rapid changes during running-in process, but remains relatively stable thereafter. As such, the surface roughness of the ring and liner samples was measured after the running-in process and found to be 0.408 and 0.571 μm, respectively. These values were then used as input parameters for the multiphysics coupling model.

The CoF and bulk temperature rise of the liner

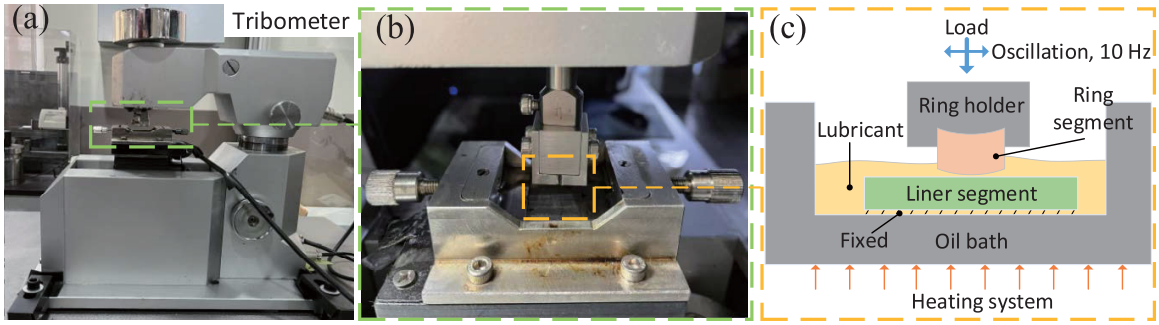

Fig. 5 Tribo-test setup used for the present study (a, b) reciprocating tribometer (MFT-R4000), and (c) schematic principle of the ring-on-liner contact.

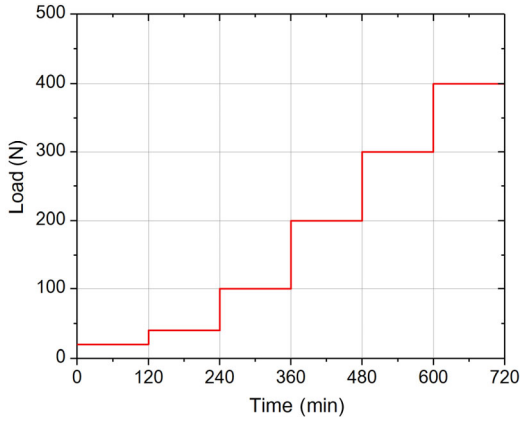

Fig. 6 Step-load sequence for the scuffing tests.

segment were continuously monitored during the tests using a force transducer and thermocouple, respectively. The CoF data was recorded by the tribometer software, while the temperature data was transmitted from the liner segment to a stationary measurement equipment using a telemetry system. The thermocouple was positioned approximately 1 mm beneath the contact surface (Fig. 3). The stepwise load addition was terminated either scuffing failure occurred or the end time was reached. In case surface scuffing was initiated, it was identified by a sudden increase in the CoF value, which exceeded 0.3.

3.3 Surface characterization

The residual oil was removed using an ultrasonic bath with anhydrous ethanol for 10 minutes after each test. To measure the wear contour map of the liner segment, a 3D laser-scanning confocal microscope (Keyence VK-X100/X200) was used, and measurements were conducted in different positions across the wear track in the middle of the stroke to avoid any contamination or possible wear debris. The final wear depth was determined by calculating the average of these measurements. The surface morphology of the liner segment after the test was observed using a scanning electron microscope (SEM, Vega Lab6-SEM). The chemical element composition of the liner segment was characterized by energy dispersive X-ray spectroscopy (EDX), and the Aztec software was used for quantitative analysis of the EDX spectra.

4 Results and discussion

The experiments were conducted following the step-load sequence (Fig. 6) under the temperatures of 60, 100, and 140 °C, which resulted in three different scuffing states. The friction force, temperature rise, and wear depth were recorded. Correspondingly, these results were also simulated using the multiphysics coupling model and they were compared with experimental results to verify this model. The scuffing load was predicted and the effects of applied load and lubricant temperature were discussed. Moreover, the role of tribofilm evolution and breakdown during scuffing process was discussed and revealed.

4.1 Model verification

Figure 7 demonstrates the simulation results obtained from the present model under a representative condition of a load of 300 N and a temperature of 140 °C during a sliding period. The sliding speed varies sinusoidally over a period, resulting in a varying oil film thickness, as shown by the blue dashed line in Fig. 7(a). This leads to a corresponding variation in the friction force, as seen in Fig. 7(b) with the green

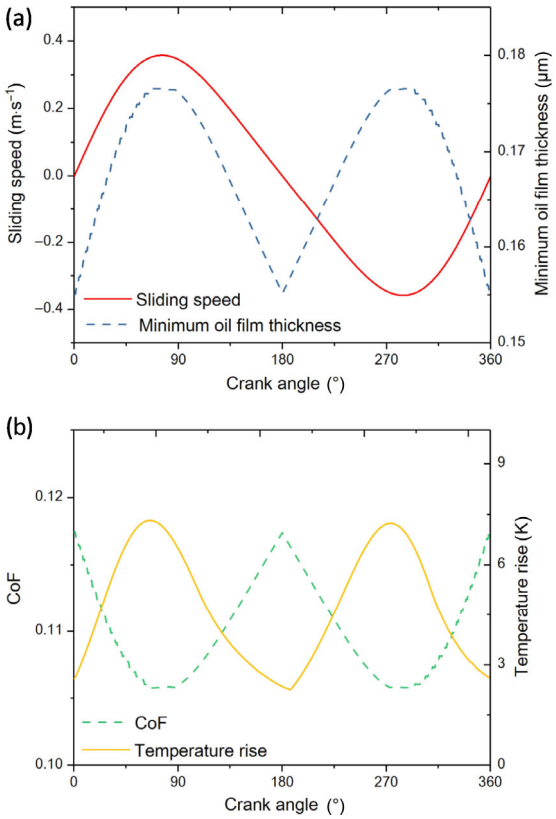

Fig. 7 Simulation results in a sliding period under a representative condition: (a) the sliding speed and minimum oil film thickness and (b) the CoF and bulk temperature rise.

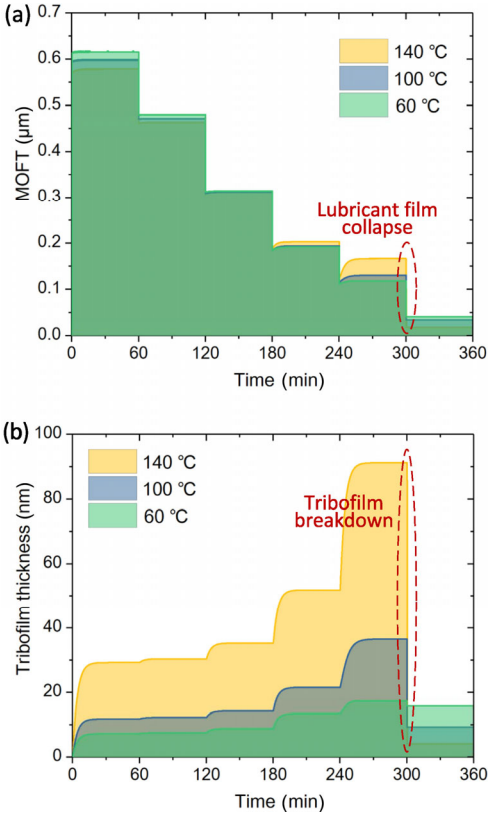

Fig. 8 Evolutions of lubricant film and tribofilm thickness with sliding time under different temperatures: (a) the minimum oil film thickness and (b) the tribofilm thickness.

dashed line. The highest friction force occurs at the two ends of the stroke, while the lowest occurs in the middle. It attributes to the varying hydrodynamic force of the oil film. The bulk temperature rise of the liner segment, shown by the yellow line in Fig. 7(b), is closely related to the sliding speed and reaches its maximum value in the middle of a stroke, where the sliding speed is the highest. The oil film thickness ratio, which is the ratio of the oil film thickness to the surface roughness (h/σ), is used to represent the lubrication state. Its maximum value is 0.22, which is significantly lower than the threshold for boundary lubrication, indicating the contact state is quite severe.

Figure 8 shows the simulated evolutions of the lubricant film and tribofilm thickness with the sliding time under different temperature conditions (60, 100, and 140 °C). Generally, the lubricant film thickness reduces at the onset of each load step due to the greater applied load. However, the thickness of the tribofilm increases following the step-load sequence before reaching the maximum load stage, and it increases significantly under higher temperature conditions, generally in an exponential manner. This observation is consistent with previous studies on ball-on-disk experiments [22, 47] and is supported by simulations using a deterministic contact model [55]. According to the stress-augmented thermal activation model (Eqs. (16) and (17)), the tribochemistry reactions producing ZDDP tribofilms are promoted by contact pressure/shear stress and lubricant temperature. Dorgham et al. [25] pointed out that a higher contact pressure/shear stress or lubricant temperature can promote the decomposition of ZDDP molecules and the polymerization of the short phosphate chains into longer ones. It is noticeable that the lubricant film thickness increases with the sliding time at the load stages of 200 and 300 N, especially under the highest temperature condition. It can be attributed to the rapid formation of ZDDP tribofilms (Fig. 8(b)). As the tribofilm grows thicker, a greater portion of the applied load is supported by the tribofilm according

to the layered statistical contact model (as discussed in Section 2.3). Consequently, the load carried by the lubricant film is reduced, leading to a slight increase in the thickness of the lubricant film. In a similar study, Azam et al. [62] investigated the influence of tribofilm on lubrication and concluded that the formation of tribofilms increased the thickness of the lubricant film and improved the lubrication regime by facilitating the entrainment of more lubricant within the contact area.

At the onset of the highest load step, the thickness of the lubricant film experiences a significant decline, and at a temperature of 140 °C, it even collapses from its highest value to its lowest. This suggests that the failure of the lubricant film is initiated by the high load and temperature. High temperature reduces the lubricant viscosity, leading to a decrease in the film's load-carrying capacity. This results in a reduction of the lubricant film thickness, leading to more asperities interacting and higher contact pressure. An increase in contact pressure can promote the formation of ZDDP tribofilms, however, if it exceeds a certain threshold, the wear/removal process of the tribofilm may become dominant [26]. Experimental results indicate that the tribofilm thickness initially increases with an increase in applied load, but it then decreases at the highest load [27]. It is believed that a moderate applied load can promote tribofilm growth, but a much higher load can inhibit its production by substantially accelerating the removal rate of the tribofilm. Gosvami et al. [26] found an unstable growth rate in single AFM tip sliding experiments when the contact pressure was higher than 5.2 GPa. Bayat et al. [28] proposed a threshold contact pressure below which the tribofilm can preserve a stable thickness, and above which tribofilm formation is suppressed, and removal becomes dominant. Moreover, higher contact loads could lead to premature failure of the protective tribofilm, as the breakdown time of the tribofilm is inversely proportional to the applied load [30]. Therefore, in this study the high contact pressure under the highest load stage significantly exacerbates the tribofilm removal process. The removal rate calculated by Eq. (14) increases rapidly and even exceeds the growth rate, causing the tribofilm thickness to decrease. Continually, the applied load born by the lubricant film will be higher, leading to a further decreasing lubricant film. Under the highest temperature (140 °C), the tribofilm removal process is the most severe due to the highest contact pressure. Consequently, a breakdown of the tribofilm occurs at the beginning of the highest load step (Fig. 8(b)).

The collapse of the lubricant film and the breakdown of the tribofilm can also be observed through the rapid increase in CoF and bulk temperature, which will be further discussed later.

Figure 9 shows the experimental and predicted CoFs varying with the sliding time under different temperature conditions (60, 100, and 140 °C). The duration of each test is 6 hours and the recorded data points represent the average of a sliding period (shown in Fig. 7). The CoFs under these different temperature conditions display quite different tendencies and they reach three distinguished scuffing states. Under the temperature of 60 °C (Fig. 9(a)), the CoF keeps increasing following the step-load sequence. Its lubrication state transits from mixed to boundary lubrication, which is in line with the Stribeck curve. Due to the low lubricant temperature, the oil film is relatively thick and surface scuffing does not emerge

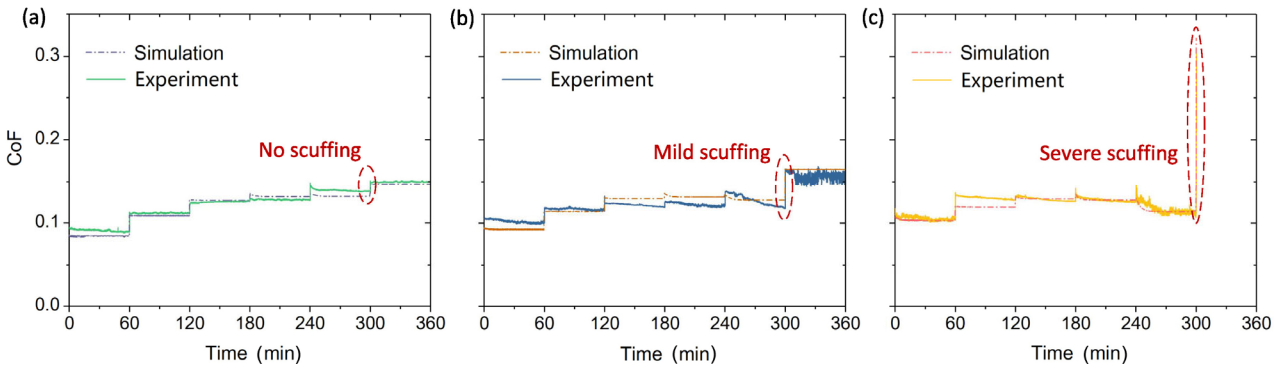

Fig. 9 Experimental and simulated CoFs under different temperature conditions: (a) 60 °C, (b) 100 °C, and (c) 140 °C.

even at the highest load stage. As the lubricant temperature increased to 100 °C, a sudden rise of CoF occurs at the beginning of the last load step and it fluctuates around 0.2 yet doesn't increase further (Fig. 9(b)). A similar CoF variation was shown in the reciprocating contact experiments by Kamps et al. [63], and an increase in excess of 100% of the CoF (from 0.11 to 0.23) is considered as a sign of the occurrence of mild scuffing [10]. It could be attributed to the accumulated wear debris as well as the tribofilm removal and the reduced lubricant film (Fig. 8). The removal of tribofilms significantly impacts the friction and lubrication of the rubbing pair [27]. When the lubricant is further heated to 140 °C, severe scuffing initiates at the beginning of the last load step and it is indicated by a rapid rise of CoF from 0.12 to 0.33 (Fig. 9(c)). In this situation, the substrate material is exposed and adhesive contact occurs due to the severe tribofilm removal process (Fig. 8). The CoFs obtained in experiments and those simulated by the multiphysics coupling model generally show similar trends with respect to sliding time across the three different scuffing states. This indicates that the current model is able to capture the onset of surface scuffing.

The bulk temperature rises of the liner segment monitored in the experiments and predicted by the present model are compared in Fig. 10. The bulk temperature where the thermocouple located is simulated based on the model shown in Fig. 3 and solved using the energy equations (Eqs. (4)–(7)). The temperature rise curve typical follows the loading scheme, with a stepwise increase in temperature. As the applied load goes higher, the bulk temperature of the liner segment first increases rapidly and then stabilizes at a higher level. The temperature rise at the highest load stage under the lubricant temperature of 60 °C is the lowest (about 8 °C), indicating no sign of scuffing. Under the temperature of 100 °C, it becomes higher and fluctuates around 10 °C due to the local adhesive contact, which is similar to the variation of CoF (Fig. 9(b)). Under the highest lubricant temperature (140 °C), adhesive contact dominates and massive friction heat is generated without the protection of the lubricant film or tribofilm. The emergence of severe scuffing can be identified by a sharp and sudden increase in the temperature curve towards the end, as depicted in Fig. 10(c). It is supposed that a high temperature rise not only decreases the lubricant viscosity to further exacerbate the lubrication state but also weakens the tribofilm mechanical properties and lowers the tribofilm wear resistance [54]. Similar bulk temperature rise curves were shown in Ref. [64] by Savolainen and Lehtovaara and they supposed that in order to cause scuffing failure, there needs to produce a highly localized frictional temperature in the contact area.

The wear contour maps of the liner segments under different temperature conditions measured by the laser-scanning confocal microscope are shown in Fig. 11. Under the temperature of 60 °C, the 3D wear contour map shows no evidence of obvious material spalling caused by adhesion, but only rows of furrows appear, which indicates that abrasive wear dominates. The 2D wear scar profile from this region exhibits a relatively smooth surface and the lowest wear depth. Similar experimental results of the PRCL contact were shown in Ref. [65]. As the temperature increased to 100 °C, the wear contour becomes rougher, and

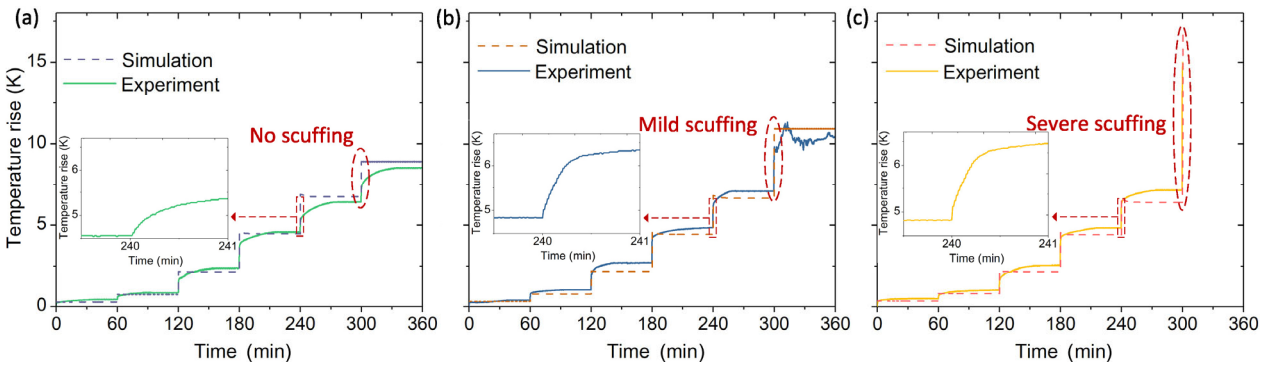

Fig. 10 Experimental and simulated bulk temperature rises of the liner segment under different temperature conditions: (a) 60 °C, (b) 100 °C, and (c) 140 °C.

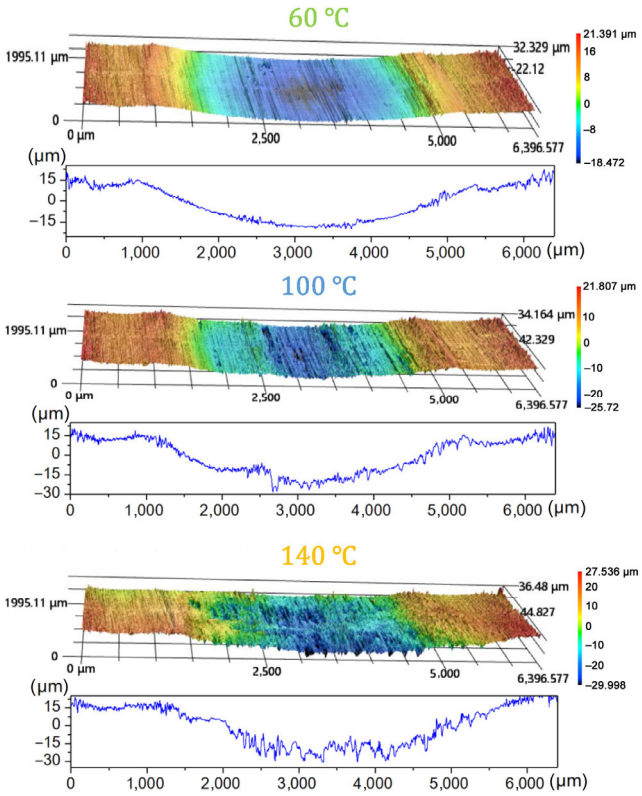

Fig. 11 Measured wear contour maps under different temperature conditions by laser-scanning confocal microscope.

some local surface craters appear, indicating the occurrence of adhesive wear. Under the temperature of 140 °C, the surface that experienced severe scuffing exhibits significantly more topographical variation. It has surface craters up to 50 μm in depth, scattered with scoring marks that align with the sliding direction. Compared to the mild wear scar, the severe wear scar displays a much rougher profile and a much deeper wear depth.

Figure 12 summarizes the predicted and measured wear depths as a function of temperature and their corresponding optical microscope images. The wear depths show an increasing trend with temperature, as observed in both the simulations and experiments. The wear depth under the temperature of 60 °C is 28 μm and it is increased to 32 μm under the temperature of 100 °C, which indicates more severe wear. Under the highest temperature (140 °C), the wear depth substantially increases to 40 μm. The wear depth results match the variations of CoF and temperature rise in Figs. 9 and 10. The optical images of the wear scar clearly show three different wear

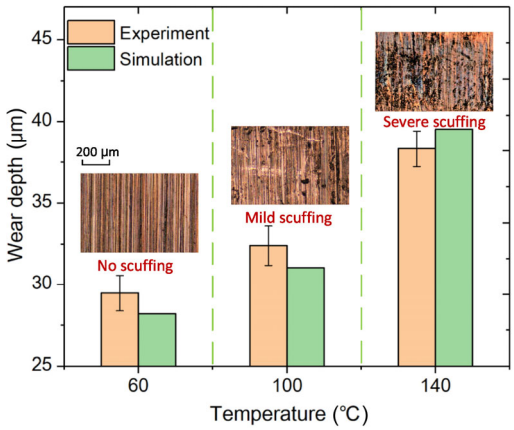

Fig. 12 Predicted and measured wear depths and the corresponding optical images under different temperatures.

states, which are marked as no scuffing, mild scuffing, and severe scuffing, and the last one presents with apparently failed regions which are consistent with the experimental data across the three different wear states, and it is capable of detecting the abrupt increase in wear depth during the transition from mild to severe scuffing. When severe scuffing occurs, the dominant wear mechanism shifts to adhesive wear because of the breakdown of the protective lubricant film and tribofilm (Fig. 8). In this situation, the wear calculated by the present wear model (Eqs. (21) and (22)) mainly stems from adhesive wear.

4.2 Scuffing analysis

In Fig. 13, SEM images of the liner segments under different temperatures reveal the wear scar characteristics. At 60 °C, abrasive wear causes rows of furrows in the sliding direction (S.D.) without evidence of scuffing or adhesive wear. Scuffing failure does not occur and there is little evidence of adhesive wear. However, as the temperature increased to 100 °C, the evidence of adhesive wear emerges locally. The SEM image shows smoothed areas with scoring craters and micro cracks parallel to the sliding direction which is similar to the wear topology (Fig. 11). The smoothed areas on the mild-scuffing surface indicate material removal from asperity peaks and filling of surface valleys, producing a polished appearance. Suh et al. [66] proposed that this process serves as a precursor to severe scuffing. Additionally, the substrate material begins to peel off from the surface in small sections, resulting in local scoring marks. The SEM

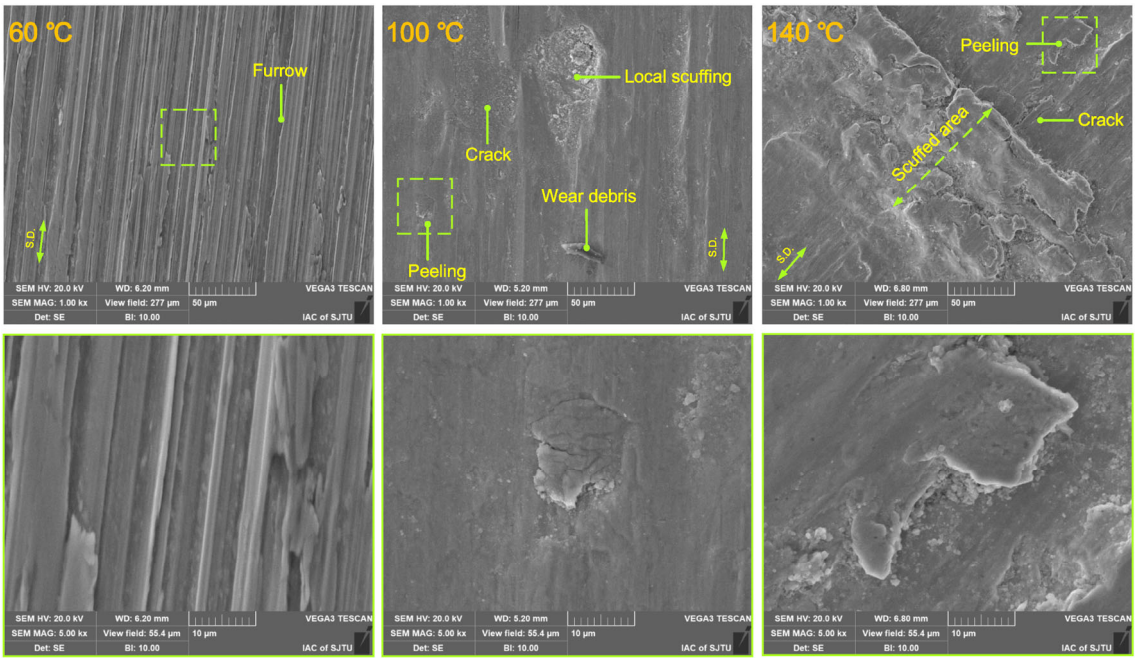

Fig. 13 SEM images of the wear scar on the liner segments under different temperatures.

image under the temperature of 140 °C shows largely scuffed areas and noticeable cracks. During the mild-scuffing process, the cracks begin to emerge on the liner segment surface, and as scuffing progresses to a severe state, these cracks propagate and form extensive 3D networks [10]. These networks facilitate the peeling off of substrate material in large sections up to 50 μm deep through adhesive contact, causing a significant increase in surface roughness across the wear scar, as shown in Fig. 11. Entrained substrate material in the contact area work hardens and causes scoring, preventing the recovery of the lubricant film and tribofilm, finally resulting in a severely scuffed surface [10].

Table 4 presents the EDX chemical composition analysis of the wear scar on the liner segments at different temperatures. It is noticeable that a higher concentration of oxygen appears under the mild and severe scuffing states (100 and 140 °C), compared with the no-scuffing state (60 °C), while the chemical compositions of S, P, Zn, which are typical elements of ZDDP molecules, are much lower or even not detected under the scuffing state. It indicates that the oxidation is quite severe and the ZDDP tribofilms attached on the surface have been removed when severe scuffing occurs (Fig. 8). In contrast, when there is no scuffing, the surface is covered with an adequate amount of lubricant that has a certain thickness. This lubricant effectively removes wear debris from the contact area, maintains a low contact temperature (as shown in Fig. 10(a)), and consequently restricts the oxidation rate [9]. Moreover, covering with ZDDP tribofilms can mitigate wear and inhibit oxidation [67]. The EDX results agree with the lubricant film and tribofilm evolutions predicted by the present model in Fig. 8. It should be noted that the EDX analysis probes to a depth of around 1–3 μm, which is much greater than the thickness of the tribofilm (usually

Table 4 EDX chemical composition of the wear scar on the liner segments under different temperatures.

Temperature (℃)	Chemical composition (at%)								
	Fe	C	O	Si	Cr	Mn	S	P	Zn
60	84.96	6.41	2.34	0.31	0.90	0.60	1.54	1.26	1.68
100	83.10	6.57	7.23	0.29	0.87	0.65	0.56	0.34	0.39
140	79.99	6.84	11.49	0.35	0.85	0.48	—	—	—

less than 200 nm). As a result, the concentrations of S, P, and Zn in the analyzed area are much lower compared to Fe.

Based on the results and discussions above, a mechanism for scuffing initiation considering the multiphysics coupling effects is proposed and its schematic illustration is shown in Fig. 14. Under mixed or boundary lubrication (Stage I), the rubbing surfaces are covered by the tribofilm generated by tribochemistry reaction. This film serves as a protective layer, preventing metal-to-metal contact between the surfaces. Additionally, there is a sufficient amount of lubricant on the surface that effectively removes wear debris from the contact area, maintains a low contact temperature (as shown in Fig. 10(a)), and consequently restricts the oxidation rate. Surface scuffing doesn't occur and abrasive wear dominates (Fig. 11). As the applied load or lubricant temperature increases (Stage II), the lubricant film becomes thinner and the tribofilm is partially removed owing to the severe contact state. The friction force and temperature rise become higher (Figs. 9(b) and 9(c)). The load is sufficiently high at this stage to cause plastic deformation of the asperity peaks on the ground surface, which then spread into the valleys, and the cracks begin to develop on the surface, Fig. 13 (100 °C). The evidence of local adhesive wear and surface scuffing emerges. At stage III, the lubricant film becomes further thinner, resulting in a more severe contact state. The tribofilm removal process is exacerbated by the high contact pressure. Its removal rate increases rapidly and even exceeds the growth rate. Then the tribofilm thickness further decreases and adhesive contact increases. Successively, the friction force and contact temperature rises significantly (Fig. 10(c)), resulting a reduced lubricant viscosity, and the load born by the lubricant film becomes higher. They both leads to a further decreased lubricant film thickness and deteriorated contact state. A high temperature rise could also weaken the tribofilm mechanical properties and lower the tribofilm wear resistance. As a result, the lubricant film collapse and tribofilm breakdown initiate and progress instantaneously in a coupling way. At the same time, the cracks propagate to form intricate networks which facilitate the peeling off of substrate material in large sections by adhesive wear (Fig. 13). It causes a significant rise in surface roughness throughout the wear scar (Fig. 11). The entrainment of large substrate material pieces into the contact area results in work hardening and scoring, thereby hindering the recovery of the lubricant film and tribofilm. As a consequence, severe scuffing occurs.

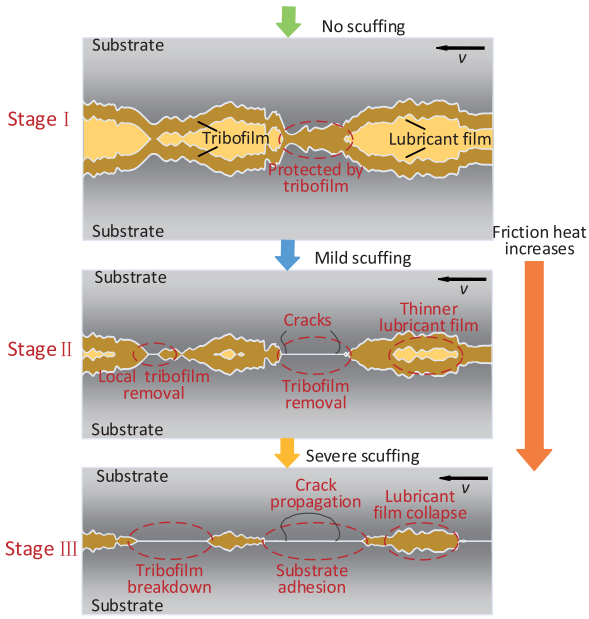

Fig. 14 Schematic illustration of severe scuffing initiation based on multiphysics coupling effects.

5 Conclusions

Modeling surface scuffing is a challenging tribological task that cannot be easily accomplished. Its initiation depends on the multiphysics coupling effects, which include hydrodynamic lubrication, asperity contact, thermal effect, tribochemistry reaction, friction, wear, etc. This study strives to model these factors comprehensively and to capture the initiation of surface scuffing. Experiments and simulations were conducted for a PRCL contact following a step-load sequence under various temperature conditions. The main results that can be summarized are as follows:

1) The experimental results and predictions obtained from the multiphysics coupling model consistently exhibit similar trends for three distinct scuffing states, thus validating the proposed model. Through analysis of the results and subsequent discussion, a mechanism for scuffing initiation is proposed, which accounts for the multidisciplinary effects. Moreover,

the role of tribofilm evolution during the scuffing process is also revealed.

2) High temperatures and extreme loads could induce the lubricant film collapse, which in turn triggers the breakdown of the tribofilm due to the significantly increased removal process. The failures of both lubricant film and tribofilm progress instantaneously in a coupling way, which finally leads to severe scuffing.

3) The progression of the scuffing state is strongly associated with the evolution of the tribofilm. Mild scuffing could deteriorate to severe scuffing once the tribofilm is completely removed, which follows by adhesive contact and surface crack propagation.

Appendix

In the GT model (Eq. (8)), the asperity geometry, as represented by Tabor's roughness parameter $\eta\beta\sigma$ and asperity slope σ/β, alters the asperity contact pressure and load share, and consequently affects the friction force. Therefore, the composite surface topographical parameters η, β and σ must be measured and calculated accurately. A tactile surface roughness tester (Mitutoyo SJ-410) was used to measure the roughness profiles of the specimen surfaces. The measurements taken from the piston ring and liner were used for the current analysis. Using the profile data collected from the surface roughness tester, the required data for Tabor's roughness parameters can be determined using the method proposed by Mccool [68]:

$$\eta_{\mathrm{s}}=\frac{1}{6\pi\sqrt{3}}\left(\frac{m_4^{\mathrm{c}}}{m_2^{\mathrm{c}}}\right) \tag{A1}$$

$$\beta_{\mathrm{s}}=\frac{3\sqrt{\pi}}{8}\sqrt{\frac{1}{m_4^{\mathrm{c}}}} \tag{A2}$$

where $m_4^{\mathrm{c}}=m_4^1+m_4^2$ and $m_2^{\mathrm{c}}=m_2^1+m_2^2$ are the composite fourth and second spectral moments of surfaces ring and liner, respectively. The spectral moments are expressed as

$$m_2=\overline{\left(\frac{\mathrm{d}z(x)}{\mathrm{d}x}\right)^2} \tag{A3}$$

$$m_4=\overline{\left(\frac{\mathrm{d}^2z(x)}{\mathrm{d}x^2}\right)^2} \tag{A4}$$

where the overbar means the average value and $z(x)$ is the roughness profile height deviation from the mean surface plane along the measuring direction. Based on the measurements and subsequent calculations, the surface topographical parameters taken into the model are listed in Table 2.

Acknowledgements

This study was supported by the National Natural Science Foundation of China (52130502, 52171315) and the National Key R&D Program of China (2022YFB4201102).

Author contributions

Conceptualization, Bugao LYU, Jiabao YIN, and Xianghui MENG; Data curation, Bugao LYU, Jiabao YIN, and Xianghui MENG; Formal analysis, Bugao LYU; Funding acquisition, Xianghui MENG; Investigation, Bugao LYU and Jiabao YIN; Experiment, Bugao LYU and Jiabao YIN; Software, Bugao LYU; Supervision, Xianghui MENG, Yi CUI, and Chengen WANG. All authors have read and agreed to the published version of the manuscript.

Declaration of competing interest

The authors have no competing interests to declare that are relevant to the content of this article.

References

[1] Wang Y, Yao C, Barber G C, Zhou B, Zou Q. Scuffing resistance of coated piston skirts Run against cylinder bores. *Wear* **259**(7–12): 1041–1047 (2005)

[2] Ferreira R, Carvalho Ó, Sobral L, Carvalho S, Silva F. Laser texturing of piston ring for tribological performance improvement. *Friction* **11**(10): 1895–1905 (2023)

[3] Lyu B G, Meng X H, Zhang R, Wen C W. A deterministic contact evolution and scuffing failure analysis considering lubrication deterioration due to temperature rise under heavy loads. *Eng Fail Anal* **123**: 105276 (2021)

[4] Li H J, Tian P Y, Lu H Y, Jia W P, Du H D, Zhang X J, Li Q Y, Tian Y. State-of-the-art of extreme pressure lubrication realized with the high thermal diffusivity of liquid metal. *ACS Appl Mater Interfaces* **9**(6): 5638–5644 (2017)

[5] Blok H. Surface temperature measurements on gear teeth under extreme pressure lubricating condition. *Proc Inst Mech Eng* **2**:14–20 (1937)

[6] Dyson A. The failure of elastohydrodynamic lubrication of circumferentially ground discs. *Proc Inst Mech Eng* **190**(1): 699–711 (1976)

[7] Hershberger J, Ajayi O O, Zhang J, Yoon H, Fenske G R. Evidence of scuffing initiation by adiabatic shear instability. *Wear* **258**(10): 1471–1478 (2005)

[8] Ajayi O O, Lorenzo-Martin C, Erck R A, Fenske G R. Analytical predictive modeling of scuffing initiation in metallic materials in sliding contact. *Wear* **301**(1–2): 57–61 (2013)

[9] Saeidi F, Taylor A A, Meylan B, Hoffmann P, Wasmer K. Origin of scuffing in grey cast iron-steel tribo-system. *Mater Des* **116**: 622–630 (2017)

[10] Kamps T J, Walker J C, Wood R J, Lee P M, Plint A G. Scuffing mechanisms of EN-GJS 400-15 spheroidal graphite cast iron against a 52100 bearing steel in a PAO lubricated reciprocating contact. *Wear* **376–377**: 1542–1551 (2017)

[11] Lee B, Yu Y H, Cho Y J. A scuffing model considering additive depletion in boundary lubrication. *Ind Lubr Tribol* **72**(3): 267–272 (2019)

[12] Zhang C W, Zhai H, Sun D, Zheng D Z, Zhao X L, Gu L, Wang L Q. Thermal shock of subsurface material with plastic flow during scuffing. *Friction* **11**(1): 64–75 (2023)

[13] Hsu S M, Shen M C, Klaus E E, Cheng H S, Lacey P I. Mechano-chemical model: Reaction temperatures in a concentrated contact. *Wear* **175**(1–2): 209–218 (1994)

[14] Li S, Kahraman A, Anderson N, Wedeven L D. A model to predict scuffing failures of a ball-on-disk contact. *Tribol Int* **60**: 233–245 (2013)

[15] Castro J, Seabra J. Scuffing and lubricant film breakdown in FZG gears Part I. Analytical and experimental approach. *Wear* **215**(1–2): 104–113 (1998)

[16] Chen Y, Renner P, Liang H. A review of current understanding in tribochemical reactions involving lubricant additives. *Friction* **11**(4): 489–512 (2023)

[17] Ma Z Y, Huang R X, Yuan X S, Shen Y, Xu J J. Tribological performance and scuffing behaviors of several automobile piston rings mating with chrome-plated cylinder liner. *Friction* **10**(8): 1245–1257 (2022)

[18] Spikes H. The history and mechanisms of ZDDP. *Tribol Lett* **17**(3): 469–489 (2004)

[19] Buyanovskii I A, Samusenko V D, Strelnikova S S, Shcherbakov Y I. Boundary lubrication by a chemically modified layer. *J Mach Manuf Reliab* **51**(6): 532–539 (2022)

[20] Barnes A M, Bartle K D, Thibon V R A. A review of zinc dialkyldithiophosphates (ZDDPS): Characterisation and role in the lubricating oil. *Tribol Int* **34**(6): 389–395 (2001)

[21] Lei X, Zhang Y J, Zhang S M, Yang G B, Zhang C L, Zhang P Y. Study on the mechanism of rapid formation of ultra-thick tribofilm by CeO_2 nano additive and ZDDP. *Friction* **11**(1): 48–63 (2023)

[22] Zhang J, Spikes H. On the mechanism of ZDDP antiwear film formation. *Tribol Lett* **63**(2): 1–15 (2016)

[23] Čoga L, Akbari S, Kovač J, Kalin M. Differences in nano-topography and tribochemistry of ZDDP tribofilms from variations in contact configuration with steel and DLC surfaces. *Friction* **10**(2): 296–315 (2022)

[24] Liu K, Kang J J, Zhang G G, Lu Z B, Yue W. Effect of temperature and mating pair on tribological properties of DLC and GLC coatings under high pressure lubricated by MoDTC and ZDDP. *Friction* **9**(6): 1390–1405 (2021)

[25] Dorgham A, Azam A, Morina A, Neville A. On the transient decomposition and reaction kinetics of zinc dialkyldithiophosphate. *ACS Appl Mater Interfaces* **10**(51): 44803–44814 (2018)

[26] Gosvami N N, Bares J A, Mangolini F, Konicek A R, Yablon D G, Carpick R W. Mechanisms of antiwear tribofilm growth revealed *in situ* by single-asperity sliding contacts. *Science* **348**(6230): 102–106 (2015)

[27] Lyu B G, Zhang L M, Meng X H, Wang C G. A boundary lubrication model and experimental study considering ZDDP

tribofilms on reciprocating friction pairs. *Tribol Lett* **70**(2): 1–16 (2022)

[28] Bayat R, Lehtovaara A. Tribofilm formation of simulated gear contact along the line of action. *Tribol Lett* **69**(4): 1–11 (2021)

[29] Westerfield C, Agnew S. IR study of the chemistry of boundary lubrication with high temperature and high pressure shear. *Wear* **181–183**: 805–809 (1995)

[30] Nehme G, Mourhatch R, Aswath P B. Effect of contact load and lubricant volume on the properties of tribofilms formed under boundary lubrication in a fully formulated oil under extreme load conditions. *Wear* **268**(9–10): 1129–1147 (2010)

[31] Ueda M, Kadiric A, Spikes H. Influence of PMA on the anti-scuffing properties of AW/EP additives. *Tribol Int* **174**: 107756 (2022)

[32] Ueda M, Spikes H, Kadiric A. *In-situ* observation of the effect of the tribofilm growth on scuffing in rolling-sliding contact. *Tribol Lett* **70**(3): 1–21 (2022)

[33] Patir N, Cheng H S. An average flow model for determining effects of three-dimensional roughness on partial hydrodynamic lubrication. *J Lubr Technol* **100**(1): 12–17 (1978)

[34] Patir N, Cheng H S. Application of average flow model to lubrication between rough sliding surfaces. *J Lubr Technol* **101**(2): 220–229 (1979)

[35] Wu C W, Zheng L Q. An average Reynolds equation for partial film lubrication with a contact factor. *J Tribol* **111**(1): 188–191 (1989)

[36] Ausas R, Ragot P, Leiva J, Jai M, Bayada G, Buscaglia G C. The impact of the cavitation model in the analysis of microtextured lubricated journal bearings. *J Tribol* **129**(4): 868–875 (2007)

[37] Jakobsson B. The finite journal bearing, considering vaporization. *Transactions of Chalmers University of Technology* **190** (1957)

[38] Olsson K. Cavitation in dynamically loaded bearings. *Transactions of Chalmers University of Technologie* **308** (1965)

[39] Qiu Y, Khonsari M M. On the prediction of cavitation in dimples using a mass-conservative algorithm. *J Tribol* **131**(4): 1 (2009)

[40] Harigaya Y, Suzuki M, Toda F, Takiguchi M. Analysis of oil film thickness and heat transfer on a piston ring of a diesel engine: Effect of lubricant viscosity. *J Eng Gas Turbines Power* **128**(3): 685–693 (2006)

[41] Roelands C J A, Winer W O, Wright W A. Correlational aspects of the viscosity-temperature-pressure relationship of lubricating oils (Dr in dissertation at Technical University of Delft, 1966). *J Lubr Technol* **93**(1): 209–210 (1971)

[42] Gu C X, Meng X H, Xie Y B, Fan J Z. A thermal mixed lubrication model to study the textured ring/liner conjunction. *Tribol Int* **101**: 178–193 (2016)

[43] Yang P, Wang J, Kaneta M. Thermal and non-newtonian numerical analyses for starved EHL line contacts. *J Tribol* **128**(2): 282–290 (2006)

[44] Greenwood J A, Tripp J H. The contact of two nominally flat rough surfaces. *Proc Inst Mech Eng* **185**(1): 625–633 (1970)

[45] Pereira G, Munoz-Paniagua D, Lachenwitzer A, Kasrai M, Norton P R, Capehart T W, Perry T A, Cheng Y T. A variable temperature mechanical analysis of ZDDP-derived antiwear films formed on 52100 steel. *Wear* **262**(3–4): 461–470 (2007)

[46] Ghanbarzadeh A, Parsaeian P, Morina A, Wilson M C T, Eijk M C P, Nedelcu I, Dowson D, Neville A. A semi-deterministic wear model considering the effect of zinc dialkyl dithiophosphate tribofilm. *Tribol Lett* **61**(1): 1–15 (2015)

[47] Zhang J, Ewen J P, Ueda M, Wong J S S, Spikes H A. Mechanochemistry of zinc dialkyldithiophosphate on steel surfaces under elastohydrodynamic lubrication conditions. *ACS Appl Mater Interfaces* **12**(5): 6662–6676 (2020)

[48] Chen Z, Gu C J, Tian T. Modeling of formation and removal of ZDDP tribofilm on rough surfaces. *Tribol Lett* **69**(1): 1–9 (2021)

[49] Bowden, F P, Leben, L. The friction of lubricated metals. *Phil Trans R Soc Lond A* **239**(799): 1–27 (1940)

[50] Bec S, Tonck A, Georges J M, Coy R C, Bell J C, Roper G W. Relationship between mechanical properties and structures of zinc dithiophosphate anti-wear films. *Proc R Soc Lond A* **455**(1992): 4181–4203 (1999)

[51] Aktary M, McDermott M, McAlpine G A. Morphology and nanomechanical properties of ZDDP antiwear films as a function of tribological contact time. *Tribol Lett* **12**: 155–162 (2002)

[52] Taylor R I. Tribology and energy efficiency: From molecules to lubricated contacts to complete machines. *Faraday Discuss* **156**: 361 (2012)

[53] Demmou K, Bec S, Loubet J L, Martin J M. Temperature effects on mechanical properties of zinc dithiophosphate tribofilms. *Tribol Int* **39**(12): 1558–1563 (2006)

[54] Tse J S, Song Y, Liu Z X. Effects of temperature and pressure on ZDDP. *Tribol Lett* **28**(1): 45–49 (2007)

[55] Akchurin A, Bosman R. A deterministic stress-activated model for tribo-film growth and wear simulation. *Tribol Lett* **65**(2): 1–9 (2017)

[56] Roshan R, Priest M, Neville A, Morina A, Xia X, Warrens C P, Payne M J. Friction modelling in boundary lubrication

considering the effect of MoDTC and ZDDP in engine oils. *Tribol Online* **6**(7): 301–310 (2011)

[57] Archard J F. Contact and rubbing of flat surfaces. *J Appl Phys* **24**(8): 981–988 (1953)

[58] Ueda M, Kadiric A, Spikes H. Influence of steel surface composition on ZDDP tribofilm growth using ion implantation. *Tribol Lett* **69**(2): 1–14 (2021)

[59] Marx N, Fernández L, Barceló F, Spikes H. Shear thinning and hydrodynamic friction of viscosity modifier-containing oils. part I: Shear thinning behaviour. *Tribol Lett* **66**(3): 1–14 (2018)

[60] Taylor R I, de Kraker B R. Shear rates in engines and implications for lubricant design. *Proc Inst Mech Eng Part J J Eng Tribol* **231**(9): 1106–1116 (2017)

[61] Ueda M, Kadiric A, Spikes H. On the crystallinity and durability of ZDDP tribofilm. *Tribol Lett* **67**(4): 1–13 (2019)

[62] Azam A, Dorgham A, Parsaeian P, Morina A, Neville A, Wilson M C T. The mutual interaction between tribochemistry and lubrication: Interfacial mechanics of tribofilm. *Tribol Int* **135**: 161–169 (2019)

[63] Kamps T J, Walker J C, Wood R J, Lee P M, Plint A G. Reproducing automotive engine scuffing using a lubricated reciprocating contact. *Wear* **332–333**: 1193–1199 (2015)

[64] Savolainen M, Lehtovaara A. An experimental investigation of scuffing initiation due to axial displacement in a rolling/sliding contact. *Tribol Int* **119**: 688–697 (2018)

[65] Liu Z, Liang F X, Zhai L M, Meng X H. A comprehensive experimental study on tribological performance of piston ring–cylinder liner pair. *Proc Inst Mech Eng Part J J Eng Tribol* **236**(1): 184–204 (2022)

[66] Suh A Y, Polycarpou A A, Conry T F. Detailed surface roughness characterization of engineering surfaces undergoing tribological testing leading to scuffing. *Wear* **255**(1–6): 556–568 (2003)

[67] Lin Y C, So H. Limitations on use of ZDDP as an antiwear additive in boundary lubrication. *Tribol Int* **37**(1): 25–33 (2004)

[68] McCool J I. Relating profile instrument measurements to the functional performance of rough surfaces. *J Tribol* **109**(2): 264–270 (1987)

Bugao LYU. He received his bachelor's degree in the School of Mechanical and Storage Engineering in 2018 from China University of Petroleum-Beijing, China. After then, he is a Ph.D. student in the School of Mechanical Engineering at Shanghai Jiao Tong University, China. His research interests include boundary lubrication, surface scuffing and online measurement. He has published 5 papers on international engineering journals.

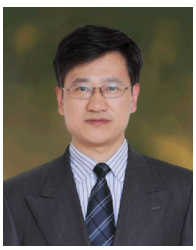

Xianghui MENG. He received his bachelor's and master's degrees in 1995 and 1999, respectively, from Xi'an Jiao Tong University, China, and Ph.D. degree in 2006 from Shanghai Jiao Tong University, China. He was invited to visit the Massachusetts Institute of Technology (MIT), USA, during 2011–2012. His current position is a professor and doctorial supervisor at School of Mechanical Engineering, Shanghai Jiao Tong University. His research areas cover the tribological simulation, online measurement and low friction design of complex mechanical products. He has presided many research projects such as the Key Program of National Natural Science Foundation of China and has published more than 70 papers on international engineering journals.